J Sol-Gel Sci Technol (2017) 83:229–236
DOI 10.1007/s10971-017-4404-1

ORIGINAL PAPER: SOL-GEL, HYBRIDS AND SOLUTION CHEMISTRIES

The effect of synthesis medium on structure and drug delivery behavior of CTAB-assisted sol–gel derived nanoporous calcium–magnesium–silicate

Sadegh Ghadiri[1] · S. A. Hassanzadeh-Tabrizi[2] · Ashkan Bigham[1]

Received: 22 March 2017 / Accepted: 1 May 2017 / Published online: 10 May 2017

Abstract In the present study, mesoporous calcium–magnesium–silicate was prepared via cetyltrimethylammonium bromide (CTAB)-assisted sol–gel method in both acidic and alkaline mediums. The effects of synthesis medium on structural properties, and drug delivery behavior of mesoporous calcium–magnesium–silicate by using ibuprofen as model drug are investigated. The X-ray diffraction results of the samples calcined at 600 °C showed that the sample synthesized at alkaline environment is composed of $CaSiO_3$ and $CaMgSiO_4$ phases, whereas in acidic condition the sample consists of akermanite, $CaMgSiO_4$, $CaSiO_3$, and MgO. The specific surface area of the mesoporous calcium–magnesium–silicate samples prepared in acidic and alkaline conditions were 220 and 140 m^2/g, respectively. The mesoporous calcium–magnesium–silicate sample synthesized in the acidic condition resulted in smaller particles with a size ranging between 50 and 100 nm. Encapsulation of ibuprofen into mesoporous calcium–magnesium–silicate was studied as a function of time.

Graphical Abstract

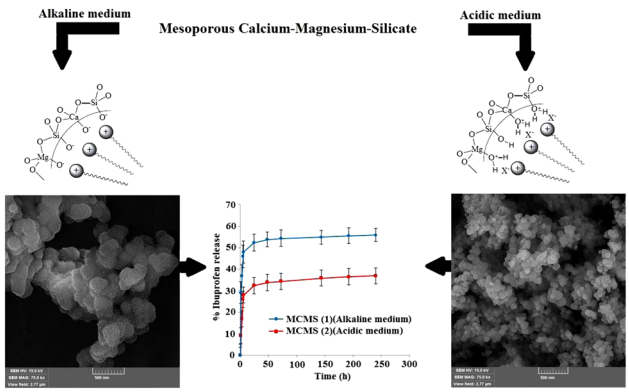

Keywords Sol–gel · Drug delivery · Mesoporous · Calcium–magnesium–silicate · Ibuprofen

1 Introduction

Bioactive ceramics (BCs) demonstrate many of the properties which make them an ideal candidate for bone grafting and scaffolding [1]. The implantation of BCs into bone defects provides structural and functional solutions to the patient bone. However, the problem with the bone implant and scaffold materials is infection, which is attributed to bacterial adhesions on implant surface, after the surgery. When colonization by infectious micro-organisms takes place, systemic administration of antibiotics does not always reach efficient concentrations at the infection site, mainly due to poor blood flow in the bone tissue. In that case, large antibiotic doses are needed, with the subsequent

✉ S. A. Hassanzadeh-Tabrizi
tabrizi1980@gmail.com
hassanzadeh@pmt.iaun.ac.ir

[1] Advanced Materials Research Center, Department of Materials Engineering, Najafabad Branch, Islamic Azad University, Najafabad, Iran

[2] Young Researchers and Elite Club, Najafabad Branch, Islamic Azad University, Najafabad, Iran

drawbacks to the rest of the body. These infections become serious if it is not treated properly and leads to revision of surgeries [2, 3]. Therefore, one of the most effective strategies consists of filling the bone defect with a drug-loaded BCs, which has the capability to release anti-inflammatory or anti-biotic drugs locally. The cooperation of both the bioactivity and the capability of BCs for local drug delivery is an outstanding perspective for bone therapy purposes [4].

It is proved by many researchers that a series of materials consist of calcium–magnesium–silicate possess good biocompatibility and bioactivity. Wang et al. indicated that nanoporous $CaO–MgO–SiO_2–P_2O_5$ materials have excellent bioactivity and were potential biomaterials for bone substitute [5]. Another study exhibited that no cytotoxicity of the diopside ($CaMgSi_2O_6$) bioceramic against the osteogenic cell line is shown during in vitro experiments, and the prepared-implants formed a strong bond to the bone via an apatite layer in vivo [6]. The akermanite ($Ca_2MgSi_2O_7$) and bredigite ($Ca_7MgSi_4O_{16}$) bioceramics by production of Ca^{2+}, Mg^{2+}, and Si^{4+} ions could stimulate osteoblast proliferation and differentiation and support human osteoblastic-like cell attachment. Moreover, it is reported that these materials are also biodegradable and have the ability of apatite formation on their surfaces in a simulated body fluid (SBF) [7].

In the last two decades, inorganic mesoporous materials (IMM) with pore sizes in the range of 2–50 nm have attracted significant attention due to their structural characteristics including their uniform pore size distribution, high specific surface area, high pore volume, and tunable pore size, encompassing the main characteristics required for application as bioactive materials. In addition, supramolecular chemistry has allowed for the design and synthesis of IMM with fascinating textural and structural features that open many paths for the research on bioactive materials for bone tissue regeneration [1, 4]. So far, various surfactant-assisted methods in order to produce IMM have been developed [8, 9]. Huo et al. [8] revealed that cetyltrimethylammonium bromide (CTAB)-assisted sol–gel synthesis of IMM in the basic medium involves direct cocondensation of anionic inorganic species with a cationic surfactant in the S^+I^- pathway ($I^- =$ silica species and $S^+ =$ cationic surfactant). By contrast, the same method in order to synthesize IMM in the acid medium involves condensation of ionic inorganic species in the presence of similarly charged surfactant molecules, this $S^+X^-I^+$ pathway is mediated by counterions of opposite charge to that of the surfactant head group ($I^+ =$ silica species, $S^+ =$ cationic surfactant and $X^- =$ counterion). It should be noted that the synthesis by the S^+I^- route is different from that by the $S^+X^-I^+$ route. As Stucky et al. suggested [10], when the ammonium surfactant S^+ is used as a templating agent in the synthesis of IMM, the acid anion X^- plays a key role in this route, as it serves to buffer the repulsion between the I^+ and the S^+ by means of weak hydrogen bonding forces in acidic conditions. Thus the $S^+X^-I^+$ route can offer more versatile structures and morphologies than the S^+I^- route, due to its weaker surfactant/silicate interaction in $S^+X^-I^+$, the association of S^+X^- determines the structure and morphology of IMM.

In the current study, we prepared mesoporous calcium–magnesium–silicate (MCMS) via CTAB-assisted sol–gel method for the first time in both acidic and alkaline mediums. In addition, the effects of synthesis medium on structural properties, and also drug delivery behavior of MCMS by using ibuprofen as model drug are assessed.

2 Experimental procedure

2.1 Materials

Calcium nitrate tetrahydrate ($Ca(NO_3)_2{\cdot}4H_2O$), magnesium nitrate hexahydrate ($Mg(NO_3)_2{\cdot}6H_2O$), tetraethylorthosilicate (TEOS), ethanol, HCl (37 wt.%), NH_4OH (25 wt.%), and CTAB as a surfactant are purchased from Merck, Germany. All the chemicals were of reagent grade and used without further purification.

2.2 Methods

The synthesis is based on the employment of CTAB as mesostructure directing agent and it is carried out in alkaline medium with the following conditions: 2.62 g CTAB is dissolved in the mixture of ethanol, NH_4OH, and H_2O. The solution is stirred until all surfactant is dissolved. Then, the $Mg(NO_3)_2{\cdot}6H_2O$ and $Ca(NO_3)_2{\cdot}4H_2O$ are added, followed by the dropwise addition of TEOS. The final molar ratios of MCMS, which is synthesized in this study, are based on akermanite ($Ca_2MgSi_2O_7$) (1TEOS/0.3CTAB/0.5Mg$(NO_3)_2{\cdot}6H_2O$/1$Ca(NO_3)_2{\cdot}4H_2O$/10ethanol/11NH_4OH/150H_2O). After continuous stirring for 24 h, the solution is filtered and rinsed with deionized water and dried for 1 day at ambient conditions and finally in the oven overnight at 100 °C.

The synthesis of the sample in acidic medium follows the same steps. A total of 2.62 g of CTAB is dissolved in an acidic aqueous solution composed of H_2O, ethanol, and HCl aqueous solution (37 wt.%). The mixture is stirred for a few minutes before adding $Mg(NO_3)_2{\cdot}6H_2O$, $Ca(NO_3)_2{\cdot}4H_2O$, followed by the dropwise addition of TEOS. The final molar ratios are (1TEOS/0.3CTAB/0.5$Mg(NO_3)_2.6H_2O$/1$Ca(NO_3)_2.4H_2O$/10ethanol/14HCl/150H_2O). The filtering and the double drying processes are the same as in the sample, which is prepared in alkaline medium. Eventually, the synthesized MCMS samples are calcined at 600 °C at a

rate of 1 °C min^{-1} for 5 h to remove the surfactant template in the atmosphere. The samples, which are synthesized in alkaline and acidic mediums, are named as MCMS (1) and MCMS (2), respectively.

2.3 Characterization

The MCMS samples are characterized by powder X-ray diffraction (XRD) in a Philips TW3710 X 'Pert diffractometer equipped with CuKα (40 kV, 20 mA). The N_2 adsorption/desorption analyses are carried out at −196 °C on a NOVA-2000 automated gas sorption system. In both cases, 80 mg of material is degassed at 150 °C for 24 h under a vacuum lower than 0.3 kPa before the analysis. The surface area is determined using the Brunauer–Emmett–Teller (BET) method and the pore-size distributions are calculated from the adsorption branch of the isotherms by using Barrett–Joyner–Halenda method. The morphologies and elemental analysis of MCMS samples are identified using a Mira 3-XMU field emission scanning electron microscope (FE-SEM), equipped with energy dispersive analysis of X−ray (EDAX). The Fourier transform infrared spectra (FTIR) of the samples are recorded on a JASCO6300. The amount of adsorbed and released drug by MCMS samples is monitored as a function of soaking time by UV spectroscopy (UV–Vis spectrophotometer, Optizen 3220) at 235 nm.

2.4 Ibuprofen loading and release measurements

Both samples, which are labeled as MCMS (1) and MCMS (2) are added separately into drug solutions (1 mg/ml). To load the MCMS samples, 20 ml of 20 mg solution of ibuprofen prepared in ethanol is added to each 20 mg of them. The mixtures are stirred for 24 h at room temperature to load ibuprofen molecules. Then, the obtained drug loaded samples are separated by centrifugation at 10,000 rpm for 10 min and rinsed with ethanol and distilled water (pH = 7.0) and dried at room temperature. The amount of the unloaded drug is determined by absorption spectrum at 235 nm. The encapsulation efficiency of the samples is calculated according to Eq. (1).

$$\text{Encapsulation efficiency}\,(\%) = \frac{\text{Initial drug weight} - \text{Drug weight in supernatant}}{\text{Initial drug weight}} \times 100 \quad (1)$$

Release studies are performed by soaking 10 mg drug loaded MCMS samples into 10 ml phosphate buffered saline (PBS) with the pH value of 7.4 at 37 °C under constant shaking (120 rpm). The supernatant (2 ml) is extracted at different time intervals and analyzed for ibuprofen concentration by a UV–Vis spectrophotometer at a wavelength of 235 nm and replaced with the same volume of fresh PBS with the same pH value. Fraction release ibuprofen is evaluated based on Eq. (2).

$$\text{Fraction drug release} = \frac{\text{Released amount ibuprofen at a definite time}}{\text{Amount of ibuprofen loaded into samples}} \quad (2)$$

3 Results and discussion

XRD patterns at wide angles corresponding to MCMS (1) and MCMS (2) samples calcined at 600 °C, which are synthesized in alkaline and acidic mediums, respectively, are shown in Fig. 1. The XRD pattern of MCMS (1) demonstrates the presence of calcium silicate ($CaSiO_3$, JCPDS no. 01-1029) and monticellite ($CaMgSiO_4$, JCPDS no. 011-0353) phases. On the other hand, the presence of akermanite ($Ca_2MgSi_2O_4$, JCPDS no. 01-087-0038), monticellite ($CaMgSiO_4$), calcium silicate ($CaSiO_3$) and periclase (MgO, JCPDS no. 045-0946) is detected by the MCMS (2) XRD pattern. The difference between XRD patterns of both samples can be attributed to the reaction mechanisms for acid or base catalysis. The relative rate of hydrolysis and condensation reactions, which has the most important effect on the final structures of MCMS, can be very effectively influenced by pH. The lowest reaction rate for hydrolysis of silicon-based mesoporous materials (SMM) is at pH = 7 and for condensation around 4.5. Under acid-catalyzed conditions (pH < 2) of SMM synthesis process, the hydrolysis is favored, and the condensation reactions are rate-determining. The initial molecules form first many small oligomers and particles with reactive Si–OH, Mg–OH, and Ca–OH groups, followed by formation of linear or randomly branched chains. The acid-

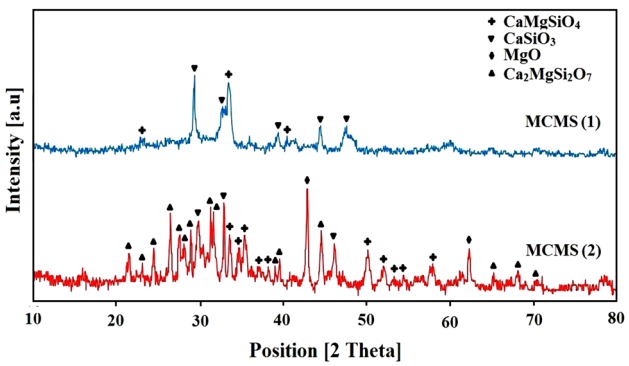

Fig. 1 Wide-angle XRD patterns of MCMS samples

catalyzed gelation is primarily characterized by a cluster–cluster growth model [11]. Generally, as a result of slower condensation reactions, more chain-like structures will be formed. So, the reason why more crystallized MCMS (2) structure is obtained after calcination at 600 °C can be attributed to slower condensation process. In contrast, above pH = 2.4, the rate of hydrolysis reaction reduces and the rate of condensation will be higher. The growth mechanism of SMM changes from cluster–cluster to monomer-cluster [12]. Therefore, more branched structures are formed rapidly, and less crystallized structures are obtained in the case of MCMS (1) at the same calcination temperature.

Figure 2 reports the IR spectra, in the 400–3900 cm^{-1} spectral range, of the MCMS (1) and MCMS (2) powder surfaces, before and after calcination process. The bands around 1640 and 3400 cm^{-1} correspond to the bending vibrations of the absorbed molecular water and the stretching vibrations of −OH groups, respectively [13, 14]. The bands between 2800 and 2950 cm^{-1} are due to the C–H stretching vibrations and the ones at 1414 and 1490 cm^{-1} [15] correspond to the bending vibrations of $-CH_2$ and $-CH_3$, exhibiting the presence and absorption of CTAB surfactant on the surfaces of both MCMS samples [13]. Calcination of MCMS samples up to 600 °C is accompanied by the disappearance of organic groups and water bands which confirms the removal of volatile components. In the 870–1100 cm^{-1} range, high-intensity bands attributed to υ_{SiO} of siloxane groups (Si–O–Si) are observed. Asymmetric stretching vibrations of Si–O–Si (υ_{SiO}) in the range of 1040–1076 cm^{-1} and bending vibrations from Si–O–Si (δ_{SiOSi}) at 533 cm^{-1} are clearly observed [16, 17]. It is worth noting that the shift of Si–O–Si peaks at 1076 and 1040 cm^{-1} in the spectras of both MCMS samples after calcination to lower wavenumbers can be attributed to strengthening of Si–O bands in the SiO_4 tetrahedron which proves the formation of crystal structures as it is shown in the XRD results (Fig. 1). In the calcined powders at 600 °C, the bands related to O–Ca–O bending modes at 420 cm^{-1} and O–Mg–O bending modes at 480 cm^{-1} are appeared. Moreover, the peak at 593 cm^{-1} shows the presence of Ca=O group [18]. The presence of water bands in the spectrum of both samples after calcination process is attributed to adsorption of water moisture by the powders from the atmosphere [16].

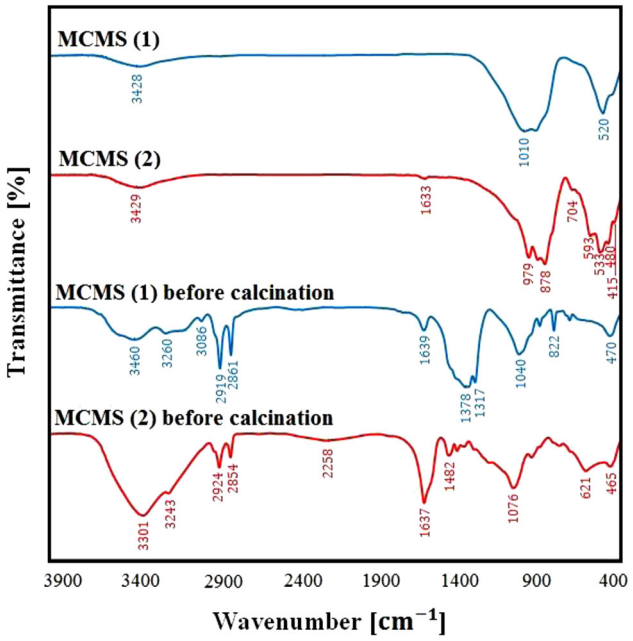

Fig. 2 FTIR spectra of MCMS samples before and after calcination

N_2 adsorption–desorption isotherms and pore size distribution curves related to MCMS (1) and MCMS (2) samples are shown in Fig. 3. The BET surface area, pore volume, and pore diameter are also listed in Table 1. It can be seen from Fig. 3 that both samples exhibit a type IV isotherm, a typical characteristic of mesoporous structures. Additionally, the type H_3 hysteresis loops are observed in both samples, feature of materials with aggregates or agglomerates particles forming slit-shape mesopores [19, 20]. As calculated from the linear part of the BET plot, MCMS (1) and MCMS (2) samples show a relatively large

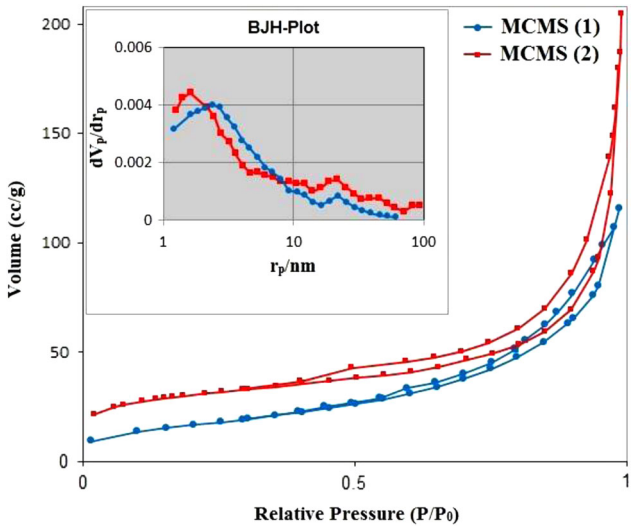

Fig. 3 Nitrogen adsorption–desorption isotherms and pore size distribution of MCMS samples

Table 1 Textural properties of MCMS samples

Sample	Surface area (m^2/g)	Pore volume (cm^3/g)	Pore diameter (nm)
MCMS (1)	140	0.24	4.3
MCMS (2)	220	0.15	2.2

specific area of 140 and 220 m^2/g, respectively. The reason why MCMS (2) sample has shown more specific surface area can be attributed to smaller particles compare to MCMS (1) sample, which lead to higher surface area to volume ratio (Fig. 4). However, MCMS (1) sample exhibits larger pore volume compare to other one which can be related to synthesis mechanism of this sample. Under alkaline conditions the condensation process is dominant over the hydrolysis, which leads to synthesis of larger particles with smaller surface area and larger pores [21].

FESEM micrographs and EDAX spectrums including quantitative results of MCMS (1) and MCMS (2) samples are presented in Fig. 4a–d, respectively. As shown in Fig. 4a, the MCMS (1) particles which are prepared in alkaline medium followed by calcination at 600 °C consisted of aggregated spherical particles with diameters about 250 nm. On the other hand, MCMS (2) shows spherical nanoparticles in range of 50–100 nm. The main difference between particle's size of these two samples can be defined through their different mechanisms. As discussed before, the hydrolysis is rate-determining in alkaline synthesis and in the presence of CTAB, inorganic species as polyanions develop direct interactions with the polar heads of CTAB. Hence, condensation of clusters with each other in the case of MCMS (1) sample is relatively fast which yields aggregated, larger, and denser particles [11, 21]. However, in acidic media, the positively charged inorganic species of MCMS (2) cannot combine directly with positive surfactant. For charge balance, there must exist a bridge counterion (X^-) at the interface of MCMS and surfactants. Therefore, these X^- ions, which mediate on the micellar interface more than in alkaline synthesis, affect the structure order and morphology of MCMS more strongly [22]. The EDAX spectrums of MCMS (1) and MCMS (2) samples confirm the presence of Si, Ca, Mg, and O elements, and validate the purity of materials.

To further assess the elements distribution on MCMS (1) and MCMS (2) samples, elemental mapping characterization is carried out. The different color images shown in Fig. 5 indicate Mg, Ca, Si, O-enriched areas of the samples.

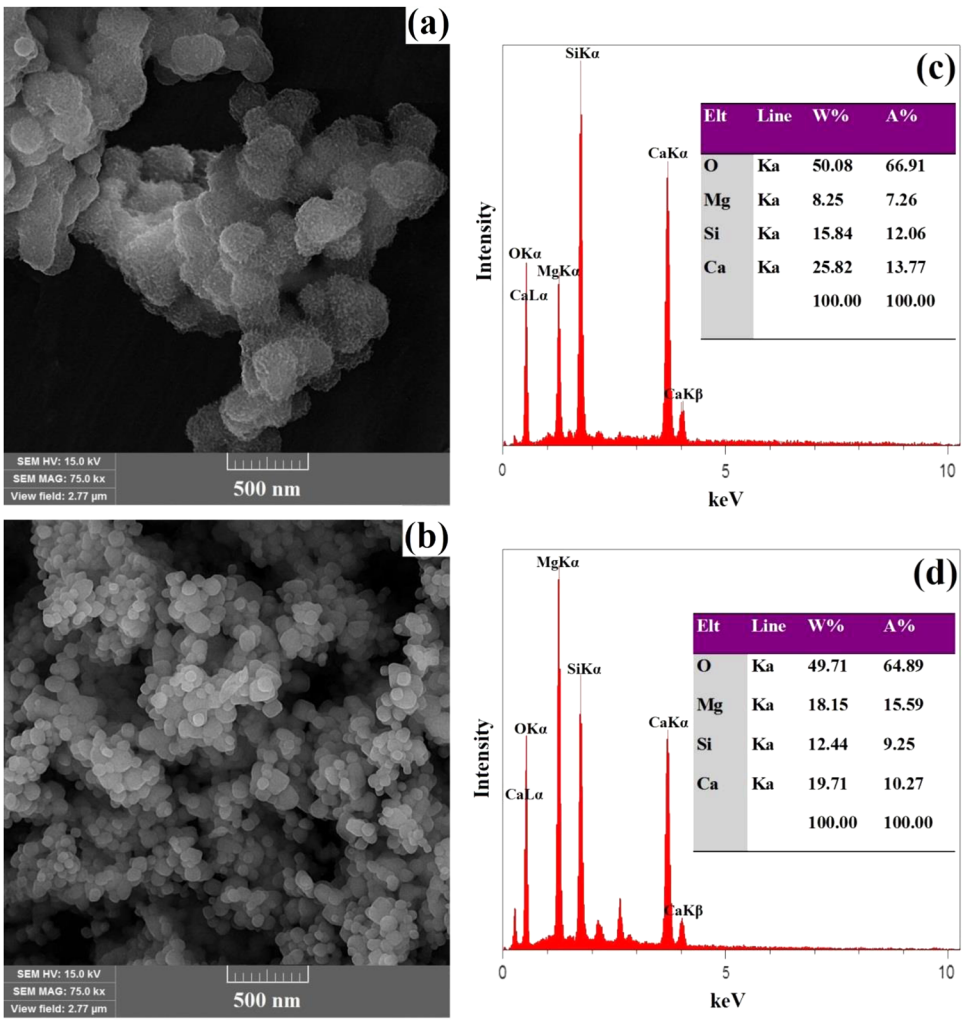

Fig. 4 FESEM micrographs of MCMS (1) (**a**), and MCMS (2) (**b**) samples; and EDAX elemental spectrum including quantitative results of MCMS (1) (**c**), and MCMS (2) (**d**) samples

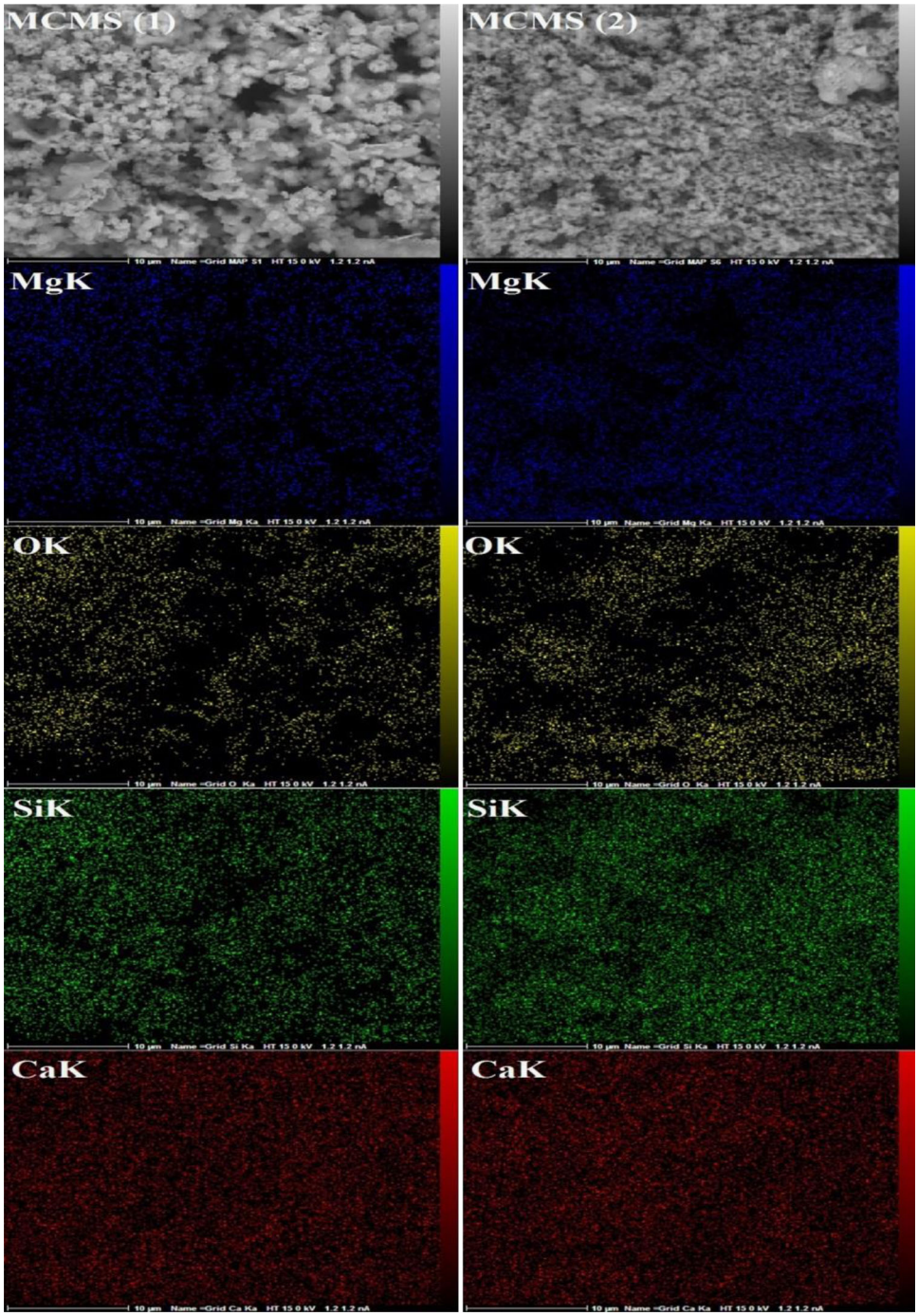

Fig. 5 Elemental mapping images of MCMS samples

It is worth noting that all elements are well dispersed on the surfaces of MCMS samples.

Ibuprofen loading is measured by using UV–Vis absorption spectroscopy at a wavelength of 235 nm to determine the drug loading capacity of the samples. The ibuprofen loading capacity of MCMS (1) and MCMS (2) samples is 530, and 620 mg/g, and the drug loading percentages of samples are 53 and 62%, respectively. The results indicate that MCMS (2) has higher ibuprofen loading compare to other sample which is attributed to its higher surface area. It is found that ibuprofen loading of both MCMS (1) and MCMS (2) samples is higher than pure silica and also amine-functionalized silica investigated by other researchers [23, 24]. It is reported by Manzano et al. [23] that MCM-41 with different morphologies loaded totally 25 wt% of ibuprofen. Moreover, they suggested that as a result of amino ($-NH_3^+$)-functionalization of carriers, the amount of loaded ibuprofen is found to increase up to 30–36%. The probable mechanism, which is discussed in their study, is attributed to electrostatic interaction between

protonated aminopropyl groups and carboxyl groups (–COOH), which leads to a stronger bonding between ibuprofen and the carrier than hydrogen one. But in our study, the same role is played with inherent modifiers. The existence of both CaO and MgO in the structure of MCMS turned this sample to a powerful adsorber of ibuprofen with acidic group. Ca and Mg belong to alkaline earth metal column of the periodic table. Thereby, CaO and MgO by creation of basic sites on the surface and pore walls of MCMS can serve as the modifier to make more effective bonding with carboxylic acid groups of ibuprofen [25, 26].

The experimental release profiles of ibuprofen from both MCMS (1) and MCMS (2) samples are shown in Fig. 6. As stated in Section 2.4 the in vitro tests are carried out by soaking ibuprofen loaded samples into a PBS solution at 37 °C and pH 7.4. Under these conditions, ibuprofen release kinetics can be assumed to be controlled by diffusion along the MCMS mesopores, since it is nearly insoluble at pH 7.4. Drug delivery is faster in the initial testing time for both MCMS (1) and MCMS (2) samples and achieves a stationary state after around 6 h. It is obvious that there are differences between drug-release rates of the samples. But both samples exhibit similar initial burst release which can be attributed to the immediate dissolution of ibuprofen located on the external surface and near the surface of them. After the initial fast release, there is a slower release of the residual bulkier drug. In the case of local drug delivery systems, the release profiles should exhibit a high initial release rate in order to respond to the elevated risk of infection from bacteria introduced during the initial shock, followed by a sustained release at an effective level for inhibiting the occurrence of latent infection [3]. The difference between release rates of MCMS (1) and MCMS (2) samples is due to the existence of two main points. First, the smaller pore diameter of MCMS (2) which obstructs the diffusion process in and out of the pores and delays the release of ibuprofen.

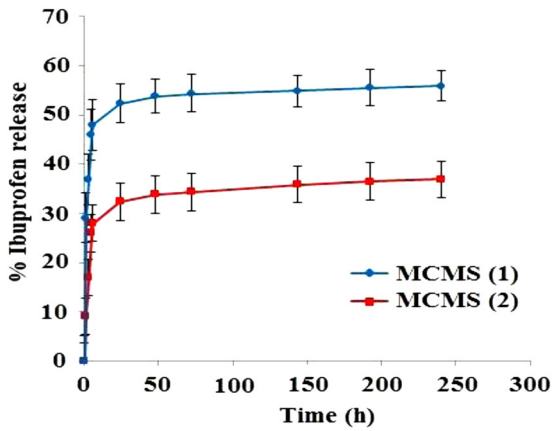

Fig. 6 Ibuprofen delivery of MCMS samples up to 240 h

The influence of pore size of IMM on drug delivery rate has been studied by Horcajada et al. [27]. They reported that the delivery rate of ibuprofen in SBF decreases as the pore size of carriers decreases. Second is related to surface area which is considered as an imperative factor in drug adsorption because this process itself is a surface phenomenon and the sample with higher surface area can load higher amount of drug molecules. Hence, it is reasonable to guess that the reverse process, release of drug molecules, would also strongly depend on the surface area. During the diffusion process, the drug molecules find more available area to interact with samples which have higher surface area, promoting extra host–guest interaction; therefore, reducing the release kinetics [28].

4 Conclusion

The MCMS was successfully obtained by CTAB-assisted sol–gel method. The effects of synthesis environments (acidic or alkaline conditions) on the structural properties and drug delivery behavior of MCMS were studied. The synthesized samples were characterized by XRD, FTIR, FESEM, elemental mapping, and UV–Vis spectroscopy. The FESEM and BET results showed that the MCMS prepared in acidic condition had smaller particle size (50–100 nm) and higher surface area (220 m^2/g) than those synthesized in alkaline medium. In addition, the ibuprofen release of the particles in PBS was investigated.

Compliance with ethical standards

Conflict of interest The authors declare that they have no competing interests.

References

1. Arcos D, Vallet-Regi M (2013) Bioceramics for drug delivery. Acta Mater 61:890–911
2. Vallet-Regi M (2014) Bio-ceramics with clinical applications. Wiley Hoboken, pp 343–359
3. Mourino V, Boccaccini AR (2010) Bone tissue engineering therapeutics: controlled drug delivery in three-dimensional scaffolds. J R Soc Interface 7:209–227
4. Vallet-Regi M, Balas F, Colilla M, Manzano M (2008) Bone-regenerative bioceramic implants with drug and protein controlled delivery capability. Prog Solid State Chem 36:163–191
5. Wang XP, Li X, Lto A, Sogo Y (2011) Synthesis and characterization of hierarchically macroporous and mesoporous $CaO–MO–SiO_2–P_2O_5$ (M = Mg, Zn, Sr) bioactive glass scaffolds. Acta Biomater 7:3638–3644
6. Wu CT, Ramaswamy Y, Zreiqat H (2010) Porous diopside ($CaMgSi_2O_6$) scaffold: a promising bioactive material for bone tissue engineering. Acta Biomater 6:2237–2245

7. Huang Y, Jin X, Zhang X, Sun H, Tu J, Tang T, Chang J, Dai K (2009) In vitro and in vivo evaluation of akermanite bioceramics for bone regeneration'. Biomaterials 30:5041–5048
8. Huo Q, Margolese DI, Ciesla U et al (1994) Generalized syntheses of periodic surfactant/inorganic composite materials'. Nature 368:317
9. Tanev PT, Pinnavaia TJ (1995) Biomimetic templating of porous lamellar silicas by vesicular surfactant assemblies. Science 267:865
10. Huo Q, Margolese DI, Ciesla U, Stucky GD et al (1994) Organization of organic molecules with inorganic molecular species into nanocomposite biphase arrays. Chem Mater 6:1176
11. Schubert U, Husing N (2005) Synthesis of inorganic materials. Wiley-VCH Weinheim, Germany. pp 192–221
12. Stolarski M, Walendziewski J, Steininger M, Pniak B (1999) Synthesis and characteristic of silica aerogels. Appl Catal A 177:139–148
13. Hassanzadeh-Tabrizi SA, Bigham A, Rafienia M (2016) Surfactant-assisted sol–gel synthesis of forsterite nanoparticles as a novel drug delivery system. Mater Sci Eng C 58:737–741
14. Tavakoli H, Sarraf-Mamoory R, Zarei AR (2015) Solvothermal synthesis of copper nanoparticles loaded on multi-wall carbon nanotubes as catalyst for thermal decomposition of ammonium perchlorate. J Adv Mater Process 3:3–10
15. Foroughi F, Hassanzadeh-Tabrizi SA, Bigham A (2016) In situ microemulsion synthesis of hydroxyapatite-$MgFe_2O_4$ nanocomposite as a magnetic drug delivery system. Mater Sci Eng C 68:774–779
16. Bigham A, Hassanzadeh-Tabrizi SA, Rafienia M, Salehi H (2016) Ordered mesoporous magnesium silicate with uniform nanochannels as a drug delivery system: The effect of calcination temperature on drug delivery rate. Ceram Int 42:17185–17191
17. Izquierdo-Barba I, Colilla M, Manzano M, Vallet-Regi M (2010) In vitro stability of SBA-15 under physiological conditions. Microporous Mesoporous Mater 132:442–452
18. Choudhary R, Koppala S, Swamiappan S (2015) Bioactivity studies of calcium magnesium silicate prepared from eggshell waste by sol–gel combustion synthesis. J Asian Ceram Soc 3:173–177
19. Zhao D, Wan Y, Zhou W (2013) Ordered mesoporous materials. Wiley, Hoboken, p 140
20. Sing KSW, Everett DH, Haul RAW, Moscou L, Pierotti RA, Rouquerol J, Siemieniewska T (2005) Reporting physisorption data for gas/solid systems with special reference to the determination of surface area and porosity. Pure Appl Chem 57:603–619
21. Sinko K (2010) Influence of chemical conditions on the nanoporous structure of silicate aerogels. Materials 3:704–740
22. Lin H, Mou C (2002) Structural and morphological control of cationic surfactant-templated mesoporous silica. Acc Chem Res 35:927–935
23. Manzano M, Aina V, Arean CO, Balas F, Cauda V, Colilla M, Delgado MR, Vallet-Regi M (2008) Studies on MCM-41 mesoporous silica for drug delivery: effect of particle morphology and amine functionalization. Chem Eng J 137:30–37
24. Gao L, Sun J, Zhang L, Wang J, Ren B (2012) Influence of different structured channels of mesoporous silicate on the controlled ibuprofen delivery. Mater Chem Phys 135:786–797
25. Shen S, Chow PS, Chen F, Tan RB (2007) Submicron particles of SBA-15 modified with MgO as carriers for controlled drug deliver. Chem Pharm Bull 55:985–991
26. Wu J, Zhu YJ, Cao SW, Chen F (2010) Hierachically nanostructured mesoporous spheres of calcium silicate hydrate: surfactant-free sonochemical synthesis and drug-delivery system with ultra high drug-loading capacity. Adv Mater 22:749–753
27. Horcajada P, Ramila A, Perez-Pariente J, Vallet-Regi M (2004) Influence of pore size of MCM-41 matrices on drug delivery rate. Microporous Mesoporous Mater 68:105–109
28. Balas F, Manzano M, Horcajada P, Vallet-Regi M (2006) Confinement and controlled release of bisphosphonates on ordered mesoporous silica-based materials. J Am Chem Soc 128:8116–8117